
FlowCast-ODE: Continuous Hourly Weather Forecasting with Dynamic Flow Matching and ODE Integration

Shuangshuang He¹ Yuanting Zhang¹ Hongli Liang¹ Qingye Meng¹ Xingyuan Yuan¹

Abstract

Accurate hourly weather forecasting is critical for numerous applications. Recent deep learning models have demonstrated strong capability on 6-hour intervals, yet achieving accurate and stable hourly predictions remains a critical challenge. This is primarily due to the rapid accumulation of errors in autoregressive rollouts and temporal discontinuities within the ERA5 data’s 12-hour assimilation cycle. To address these issues, we propose FlowCast-ODE, a framework that models atmospheric state evolution as a continuous flow. FlowCast-ODE learns the conditional flow path directly from the previous state, an approach that aligns more naturally with physical dynamic systems and enables efficient computation. A coarse-to-fine strategy is introduced to train the model on 6-hour data using dynamic flow matching and then refined on hourly data that incorporates an Ordinary Differential Equation (ODE) solver to achieve temporally coherent forecasts. In addition, a lightweight low-rank AdaLN-Zero modulation mechanism is proposed and reduces model size by 15% without compromising accuracy. Experiments demonstrate that FlowCast-ODE outperforms strong baselines, yielding lower root mean square error (RMSE) and better energy conservation, which reduces blurring and preserves more fine-scale spatial details. It also shows comparable performance to the state-of-the-art model in forecasting extreme events like typhoons. Furthermore, the model alleviates temporal discontinuities associated with assimilation cycle transitions.

1. Introduction

Accurate weather forecasting is essential for a wide range of real-world applications, including agriculture, energy management, transportation, and disaster preparedness (Bauer et al., 2015). Traditional numerical weather prediction (NWP) systems, such as the ECMWF Integrated Forecasting System (IFS), simulate atmospheric dynamics based on physical laws (Ritchie et al., 1995). These systems are computationally expensive, requiring powerful supercomputers and several hours of simulation time for multi-day forecasts (Wedi, 2014).

In recent years, deep learning-based weather forecasting models have demonstrated remarkable progress in both accuracy and efficiency (Bouallègue et al., 2024). Notable examples include FourCastNet (Pathak et al., 2022), Pangu-Weather (Bi et al., 2023), GraphCast (Lam et al., 2023), AIFS (Lang et al., 2024), and other studies (Chen et al., 2025; Nguyen et al., 2023b; Bodnar et al., 2025), which are trained on reanalysis datasets such as ERA5 (Hersbach et al., 2020) and deliver medium-range (up to 10–15 days) forecasts with skill that matches or even surpasses operational NWP systems. These models operate orders of magnitude faster than traditional NWP (Ling et al., 2024).

While deep learning has advanced the precision of weather forecasts, the prevailing 6-hour temporal resolution limits their applicability for tasks that require high-frequency temporal information (Pielke & Carbone, 2002). Training these models to produce hourly forecasts introduces two primary challenges. First, prediction errors tend to accumulate rapidly over time, resulting in unstable and unreliable forecasts (Nguyen et al., 2023a). Second, the ERA5 dataset exhibits temporal discontinuities due to its 12-hour assimilation cycle (Yuan et al., 2025), leading to notable forecast errors around 09:00–10:00 and 21:00–22:00 UTC. Training directly on hourly data forces the model to replicate these physically unrealistic jumps during those periods, resulting in the learning of incorrect dynamics and an increased accumulation of forecast errors.

Existing approaches have sought to address the challenges of hourly forecasting. Pangu-Weather (Bi et al., 2023) employs a hierarchical temporal aggregation strategy, training models

^{*}Equal contribution ¹ColorfulClouds Technology Co.,Ltd., Beijing, China. Correspondence to: Yuanting Zhang <zhangyuanting0925@gmail.com>.

at 1/3/6/24-hour intervals. The 24-hour model is utilized to suppress the fast growth of forecast errors. However, this introduces inconsistent prediction paths: for example, a 72-hour forecast relies on 3 iterations of the 24-hour model, while a 71-hour forecast involves 8 iterations of shorter-step models. Alternatively, Schreck et al. (2024) trained an hourly autoregressive model, but their forecasts display spurious high-frequency wave patterns near the tropics and Southern Ocean from day-2 onward, along with nonphysical anomalies near the poles. Hybrid physics-ML approaches such as NeuralGCM (Kochkov et al., 2024) also support hourly forecasts, but its reliance on a dynamical core to solve equations at each step slows inference compared to pure ML models.

To address these limitations, we propose FlowCast-ODE, a framework that models the temporal evolution of atmospheric states as a continuous flow. Instead of starting from noise state as in diffusion-based approaches like GenCast (Price et al.), our approach learns a conditional flow path directly from the previous timestep, aligns more naturally with the nature of weather systems (Lim et al., 2025). It also eliminates the need for explicit conditioning and reduces both training complexity and inference cost. Compared to diffusion models that require multi-step denoising and large sampling costs (Ho et al., 2020; Song et al., 2021; 2022), our approach is more straightforward and well-suited to dynamic systems with known initial conditions.

We summarize the contributions of this paper as follows: (1) *Two-Stage Training Framework for Hourly Forecasting*. We introduce a two-stage framework which performs continuous dynamic flow matching on 6-hour intervals and then leverages ODE-based fine-tuning to generate stable and coherent hourly forecasts, effectively reducing error accumulation. (2) *Addressing Temporal Discontinuities in ERA5*. We identify temporal discontinuities in ERA5 caused by its 12-hour assimilation cycle and adopt a coarse-to-fine training approach to alleviate their impact. (3) *Lightweight and Efficient Model Design*. FlowCast-ODE incorporates a low-rank AdaLN-Zero temporal modulation mechanism, reducing model parameters by approximately 15% without sacrificing accuracy. Notably, a single FlowCast-ODE model achieves the capability for hourly forecasting that previously required four separate models in Pangu-Weather.

2. Method

Problem Definition Given a spatiotemporal atmospheric field $X_k \in \mathbb{R}^{C \times H \times W}$ at time k , where C denotes the number of weather variables, the goal is to autoregressively forecast a sequence of future states $\{X_{k+1}, X_{k+2}, \dots, X_{k+N}\}$ at hourly resolution, up to a forecast horizon N (e.g., 120 hours). This task involves predicting the evolution of 71 weather variables, including 6 surface variables and 5 upper-

air variables across 13 pressure levels. The objective is to learn a model that captures the continuous dynamics of the atmosphere, enabling accurate hourly weather forecasts, while mitigating issues such as assimilation-induced discontinuities.

2.1. FlowCast-ODE Overview

As illustrated in Figure 1, FlowCast-ODE employs a two-stage training process to achieve continuous hourly weather forecasting. In the first stage, dynamical flow matching (Lim et al., 2025) is employed to learn the weather evolution at a 6-hour coarse granularity. We observe that ERA5 hourly data contain discontinuities introduced by the 12-hour assimilation cycle, often appearing as abrupt, nonphysical jumps around 09:00–10:00 and 21:00–22:00 UTC, supporting analysis can be found in Section 3.4 and Appendix A.3. Training on 6-hour intervals (00/06/12/18:00 UTC) reduces the impact of these inconsistencies, allowing the velocity model to better capture the underlying physical dynamics. We define the velocity model v_θ as the instantaneous time derivative of the atmospheric state.

$$\frac{dx(t)}{dt} = v_\theta(x_t, t, c), \quad (1)$$

where $x_t = (1-t)X_k + tX_{k+6}$, $t \in (0, 1)$ and c denotes conditioning features, includes the binary land-sea mask, geopotential at the surface, soil type, the sine and cosine of latitude and longitude, the sine and cosine of the local time of day and the year progress (all normalized to $[0, 1]$).

In the second stage, we refine forecasts to hourly resolution by integrating the learned dynamics with an explicit Euler scheme (Iserles, 2009):

$$x_{t+\Delta t} = x_t + \Delta t \cdot v_\theta(x_t, t, c), \quad (2)$$

where Δt is the integration step.

For inference, the Euler scheme is also applied to transport the input atmospheric state forward in time, producing hour-by-hour forecasts.

Overall, by combining 6-hour interval dynamic flow matching with ODE-based refinement, this two-stage framework bridges the gap between coarse 6-hour training intervals and hourly predictions, allowing the model to generate fine-grained, temporally coherent forecasts.

2.2. Dynamic Flow Matching

Flow Matching Flow Matching (Lipman et al., 2023) is a generative modeling approach based on conditional normalizing flows (Dinh et al., 2014; Chen et al., 2018) that learn time-dependent velocity fields along probability paths, enabling a continuous transformation from a simple distribution (e.g., Gaussian) to a complex target data distribution.

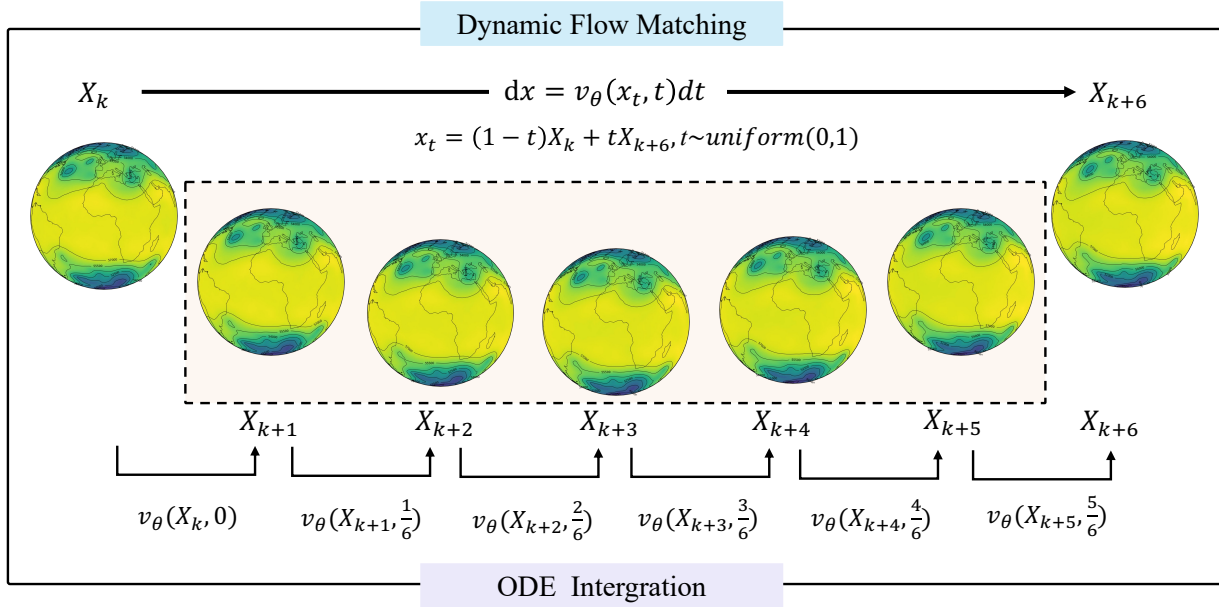


Figure 1. Overview of FlowCast-ODE. In the first stage, a velocity model v_θ is trained on 6-hour interval data pairs (X_k, X_{k+6}) to infer the velocities of intermediate states x_t for $t \in (0, 1)$. In the second stage, the model is refined with hourly data via ODE solver to achieve 1-hour temporal resolution.

The core idea is to characterize the trajectory of samples $\phi_t(x)$ over time $t \in [0, 1]$ as the solution to the differential equation:

$$\frac{d}{dt}\phi_t(x) = v_t(\phi_t(x)), \quad (3)$$

where $v_t(\cdot)$ denotes the parameterized velocity field to be learned.

The training objective minimizes the flow matching loss, which is equivalent to the conditional flow matching loss:

$$\mathcal{L}_{CFM}(\theta) = \mathbb{E}_{t, x_1, x \sim p_t(x|x_1)} \|v_t(x; \theta) - u_t(x|x_1)\|^2, \quad (4)$$

where x_1 is sampled from the target distribution. The conditional probability path is assumed Gaussian:

$$p_t(x|x_1) = \mathcal{N}(x | \mu_t(x_1), \sigma_t(x_1)^2 I), \quad (5)$$

with boundary conditions $\mu_0(x_1) = 0, \sigma_0(x_1) = 1$, corresponding to a standard Gaussian, and $\mu_1(x_1) = x_1, \sigma_1(x_1) = \sigma_{\min}$, corresponding to a narrow Gaussian around x_1 . The conditional flow transformation is:

$$\psi_t(x) = \sigma_t(x_1)x + \mu_t(x_1), \quad (6)$$

and the corresponding conditional velocity field is:

$$u_t(x|x_1) = \frac{\sigma'_t(x_1)}{\sigma_t(x_1)}(x - \mu_t(x_1)) + \mu'_t(x_1). \quad (7)$$

By reparameterizing the sample as $x_0 \sim \mathcal{N}(0, I)$, the loss becomes:

$$\mathcal{L}_{CFM}(\theta) = \mathbb{E}_{t, q(x_1), p(x_0)} \left\| v_t(\psi_t(x_0)) - \frac{d}{dt}\psi_t(x_0) \right\|^2. \quad (8)$$

In generative modeling (Liu et al., 2023; Esser et al., 2024), a commonly used path is the linear optimal transport path, which describes the process from Gaussian noise towards the target distribution through a linear conditional probability path.

$$\begin{cases} \mu_t = tx_1, \\ \sigma_t = 1 - (1 - \sigma_{\min})t, \end{cases} \quad (9)$$

with $p_t(x|x_1)$ and corresponding flow $\psi_t(x)$ and velocity field $u_t(x|x_1)$ listed in Table 1.

Dynamic Transport In meteorological forecasting and other dynamical systems, initializing from Gaussian noise often leads to a prolonged transport path, increasing model complexity when conditioning on prior time steps. To address this, we adopt a dynamic probability flow path inspired by (Lim et al., 2025), defined as:

$$\begin{cases} \mu_t = tx_1 + (1-t)x_0, \\ \sigma_t = \sigma_{\min}, \end{cases} \quad (10)$$

with $p_t(x|x_1)$ and corresponding flow $\psi_t(x)$ and velocity field $u_t(x|x_1)$ listed in Table 1. In this study, we set $\sigma_{\min} = 0$.

Table 1. Summary of Optimal Transport and Dynamic Transport

	Optimal Transport	Dynamic transport
μ_t	tx_1	$tx_1 + (1-t)x_0$
σ_t	$1 - (1 - \sigma_{\min})t$	σ_{\min}
$p_t(x x_1)$	$\mathcal{N}(x tx_1, \sigma_t(x_1)^2 I)$	$\mathcal{N}(x tx_1 + (1-t)x_0, \sigma_{\min}^2 I)$
$\psi_t(x)$	$tx_1 + (1 - (1 - \sigma_{\min})t)x$	$tx_1 + (1-t)x_0 + \sigma_{\min}x$
$u_t(x x_1)$	$\frac{x_1 - (1 - \sigma_{\min})x}{1 - (1 - \sigma_{\min})t}$	$x_1 - x_0$
$u_t(\psi_t(x_0) x_1)$	$x_1 - (1 - \sigma_{\min})x_0$	$x_1 - x_0$

Dynamic transport uses the previous time step’s atmospheric state x_0 as the starting point to transport directly to the target state x_1 . In our setting, x_0 and x_1 correspond to atmospheric fields sampled at 6-hour intervals. Although similar in form to optimal transport, the key distinction lies in the prior-informed initialization, which aligns better with physical systems and improves theoretical coherence.

2.3. Time-modulated transformer block

We adopt a 3D Swin Transformer architecture for the velocity model, with implementation details provided in the Appendix B.1. To incorporate temporal conditioning within the 3D Swin Transformer blocks, we employ an adaptive modulation mechanism inspired by the Adaptive-Zero Layer Normalization (adaLN-Zero) (Peebles & Xie, 2023). Specifically, the normalized feature representation $\tilde{\mathbf{h}}$, obtained by applying LayerNorm (Ba et al., 2016) to \mathbf{h} , is modulated by time-dependent scale $\gamma(t)$ and shift $\beta(t)$ parameters:

$$\text{adaLN}(\mathbf{h}; t) = \gamma(t) \odot \tilde{\mathbf{h}} + \beta(t) \quad (11)$$

The original adaLN-Zero mapping from the time embedding dimension t_{dim} to the hidden dimension $6C$ is full-rank, substantially increasing the parameter count. To reduce memory and computational costs, we replace this full-rank projection with a low-rank decomposition:

$$M_{t_{\text{dim}} \times 6C} \approx U_{t_{\text{dim}} \times r} V_{r \times 6C} \quad (12)$$

where $r = 32$ in this study. This reduces the total parameter count from 54.2M to 45.7M, enabling a lighter and more efficient model without compromising performance.

3. Experiments

Our experiments are built upon WeatherBench2 (Rasp et al., 2024) dataset, which comprises a subset of the fifth-generation ECMWF Reanalysis (ERA5) data. For this study, we utilize the data at a 1° , corresponding to a grid size of

181×360 . The subset employed in this study spans from 1980 to 2021, with data from 1980–2019 used for training, 2020 used for validation, and 2021 used for testing. The prediction targets include six surface-level variables and five upper-air variables at 13 pressure levels. A detailed description of the dataset, variable selection, and preprocessing methods is provided in Appendix A.1 and A.2. All training and evaluation processes were performed on 4 NVIDIA A100 GPUs, each with 40 GB of memory.

3.1. Baseline Models

Most existing AI-based weather models are designed for 6-hour forecast intervals, limiting their ability to provide high-frequency predictions. Pangu-Weather (Bi et al., 2023) addresses this by training separate models for 1-, 3-, 6-, and 24-hour forecast horizons, enabling hourly forecasts while controlling error growth over longer lead times. Its accuracy and robustness under consistent datasets and training configurations (Gao et al., 2025) make it a strong baseline for evaluating our proposed method.

We also include ClimODE (Verma et al., 2024), a physics-informed model that represents weather as a continuous-time spatiotemporal process with advection-driven, value-conserving neural flows. However, due to ClimODE running significantly slower when increasing resolution from 5.625° to 1° and is designed for only five variables, we rely on results reported in its paper. In contrast, Pangu-Weather is evaluated at a 1° resolution and trained with the same setup as our method. Thus, we adopt both Pangu-Weather and ClimODE as representative baselines to assess our approach.

3.2. Comparison with baselines

We run forecasts for FlowCast-ODE and Pangu-Weather using ERA5 reanalysis as initial conditions. Forecasts are initialized at 00Z and 12Z from 1 November to 31 December 2021, with lead times up to 120 hours. To compare error growth over long lead times, Pangu-Weather employs only its 24-hour model.

3.2.1. RMSE COMPARISON OF 5-DAY FORECASTS

The long-horizon forecast accuracy of ClimODE, Pangu-Weather, and FlowCast-ODE is compared in terms of RMSE. Figure 2 shows the latitude-weighted global mean RMSE for four surface variables (MSLP, U10M, T2M, TD2M) and four upper-air variables (Z500, U850, T850, Q850) over a 5-day forecast horizon. FlowCast-ODE achieves lower RMSE for MSLP and Z500 across all lead times. For U10M, U850, and TD2M, FlowCast-ODE outperforms both baselines at shorter lead times, with Pangu-Weather closing the gap at longer lead times, while ClimODE consistently shows higher RMSE. For Q850 and T850, FlowCast-ODE maintains an advantage over both models within the first 72 hours,

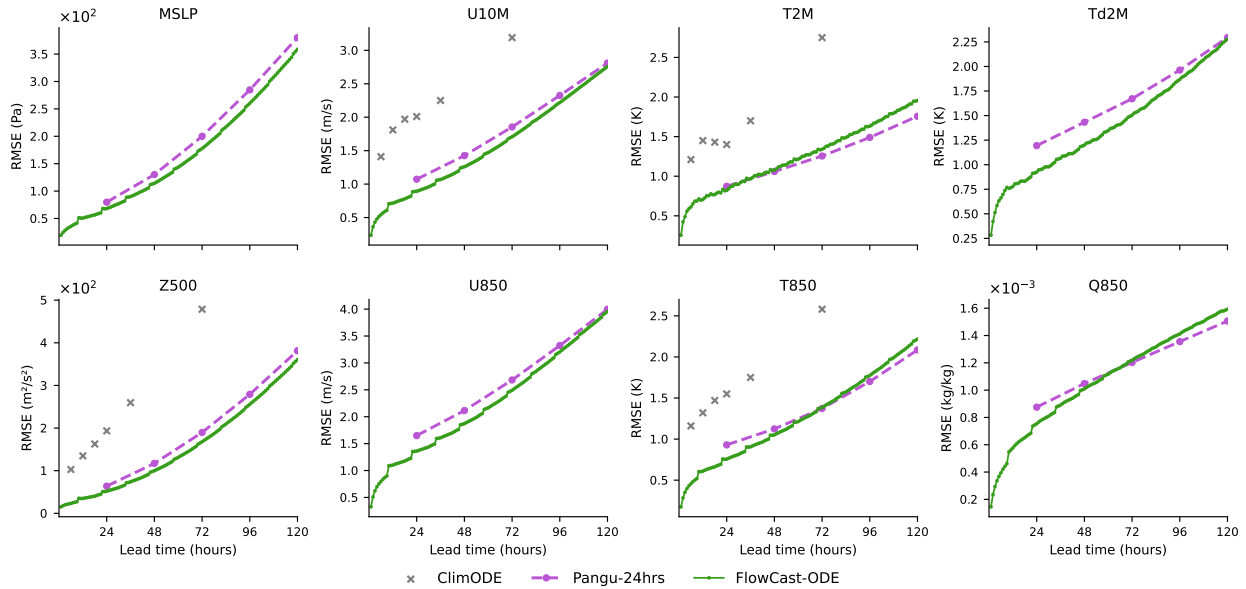


Figure 2. Comparison of latitude-weighted global mean RMSE for ClimODE (gray x markers), Pangu-Weather (24-hour intervals, purple dashed line), and FlowCast-ODE (hourly resolution, green line) across a 5-day forecast horizon. The hourly RMSE of FlowCast-ODE reveals faster error growth around 09:00–10:00 UTC and 21:00–22:00 UTC, reflecting the impact of ERA5’s 12-hour assimilation cycle on hourly model’s forecast accuracy.

after which Pangu-Weather slightly surpasses it, but both remain superior to ClimODE. For T2M, FlowCast-ODE exhibits better skill than both baselines during the first 24 hours, while Pangu-Weather performs better at longer lead times, yet both outperform ClimODE across the forecast horizon.

For the 120-hour lead time, Pangu-Weather generates forecasts by iteratively applying its 24-hour model five times, whereas FlowCast-ODE produces hourly forecasts through 120 iterations. Despite the larger number of iterations, FlowCast-ODE maintains competitive, and often superior RMSE performance, maintaining stability and low error across multiple iterations and long-horizon forecasts.

3.2.2. POWER SPECTRA

While RMSE provides a global measure of forecast accuracy, it does not reflect how well models preserve spatial structures across different scales. To evaluate this aspect, we analyze the latitude-averaged (60°N–60°S) power spectra of six variables in ERA5 for the year 2021, along with predictions from Pangu-Weather and FlowCast-ODE.

For U10, U850, and Q850, both FlowCast-ODE and Pangu-Weather underestimate power at short-to-mid wavelengths. Nonetheless, FlowCast-ODE consistently retains higher spectral energy, indicating a stronger capability to preserve fine-scale variability. For MSLP, Z500, and T2M, FlowCast-

ODE slightly overestimates short-wave energy, producing a spurious peak near wavenumber 90 that grows with lead time. As this wavenumber corresponds to the training patch size, we tentatively attribute this artifact to it and aim to address it in future work. The corresponding spectra are shown in Figure 11 (Appendix E.1).

The impact of these spectral differences is also visible in the spatial domain. As shown in Figure 3, both models reproduce the large-scale structures of ERA5 in 3-day forecasts. However, while blurring is present in both models, FlowCast-ODE better preserves spatial details, effectively reducing over-smoothing and delivering improved overall forecast accuracy compared to Pangu-Weather.

3.3. Tracking tropical cyclones

We evaluated the track forecasting performance of six representative tropical cyclones that occurred in 2021: SURIGAE, IN-FA, MINDULLE, CHANTHU, KOMPASU, and RAI. For each cyclone, predicted centers were determined by locating the MSLP minimum based on the tracking algorithm described in Appendix D.3. Observed tracks were obtained from the International Best Track Archive for Climate Stewardship (IBTrACS), which provides the most reliable reference for tropical cyclones. To provide a strong baseline, we included forecasts from the 0.25° Pangu-Weather model downloaded from WeatherBench2.

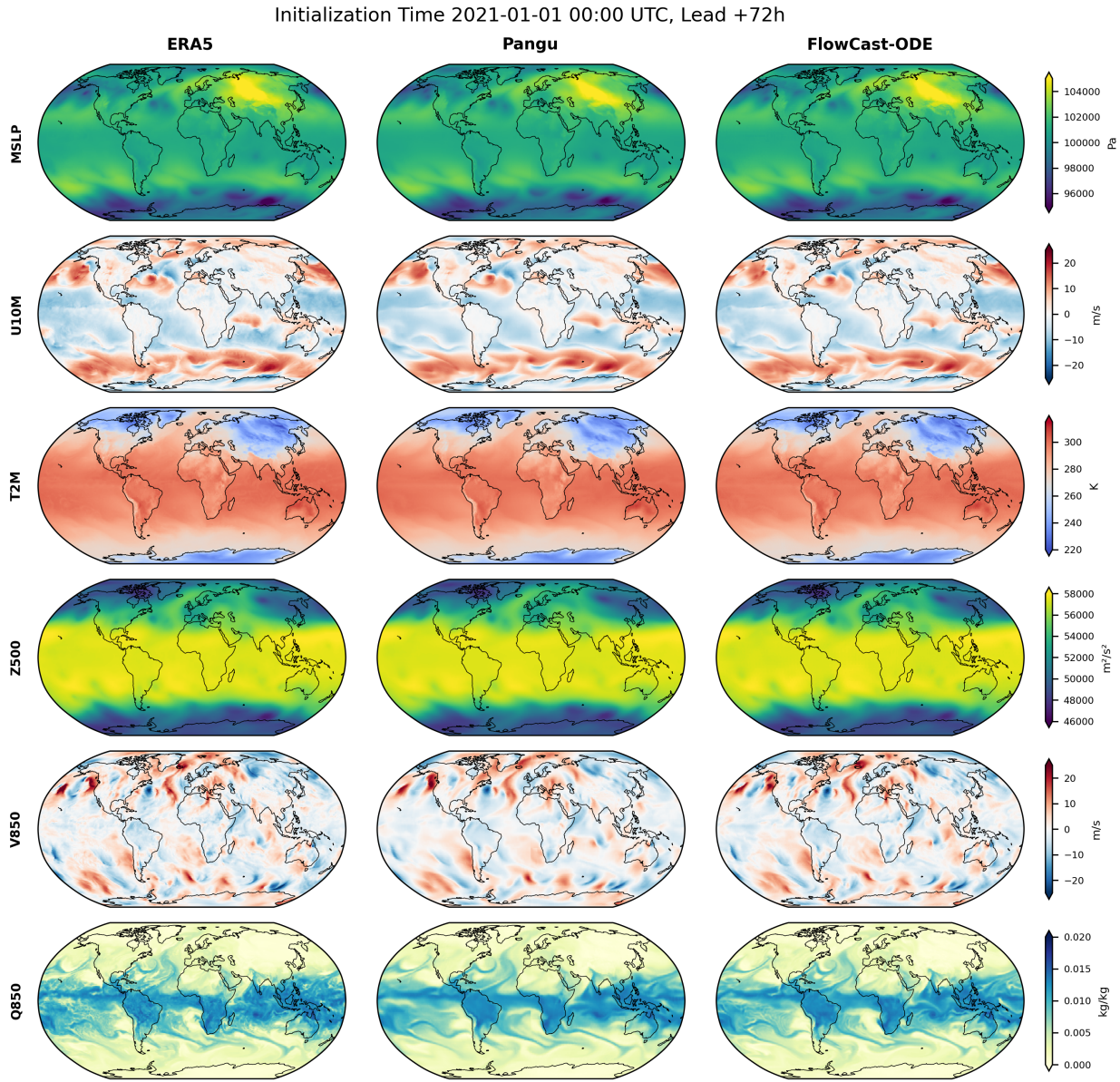


Figure 3. Visualization of 3-day forecast results for three surface variables (MSLP, U10M, T2M) and three upper-air variables (Z500, V850, Q850). For each variable, ERA5 ground truth (left), Pangu-Weather forecast (middle), and FlowCast-ODE forecast (right) are shown. Forecasts are initialized at 00:00 UTC on 1 January 2021.

Track errors were quantified using the MAE (Mean Absolute Error), representing the distance between observed and predicted cyclone centers. Figure 5 shows the MAE over the 120-hour forecast period for both FlowCast-ODE and Pangu-Weather. FlowCast-ODE generally exhibits slightly higher MAE than the 0.25° Pangu-Weather model within 48 hours, but its MAE becomes comparable to Pangu-Weather beyond 48 hours. Although FlowCast-ODE operates at a

coarser 1° resolution compared to the 0.25° Pangu-Weather model, it demonstrates competitive performance in tropical cyclone track forecasting. Figure 4 presents the observed IBTrACS tracks and corresponding five-day forecasts from FlowCast-ODE and Pangu-Weather across multiple initializations for six tropical cyclones. Both models reproduce the overall trajectory patterns.

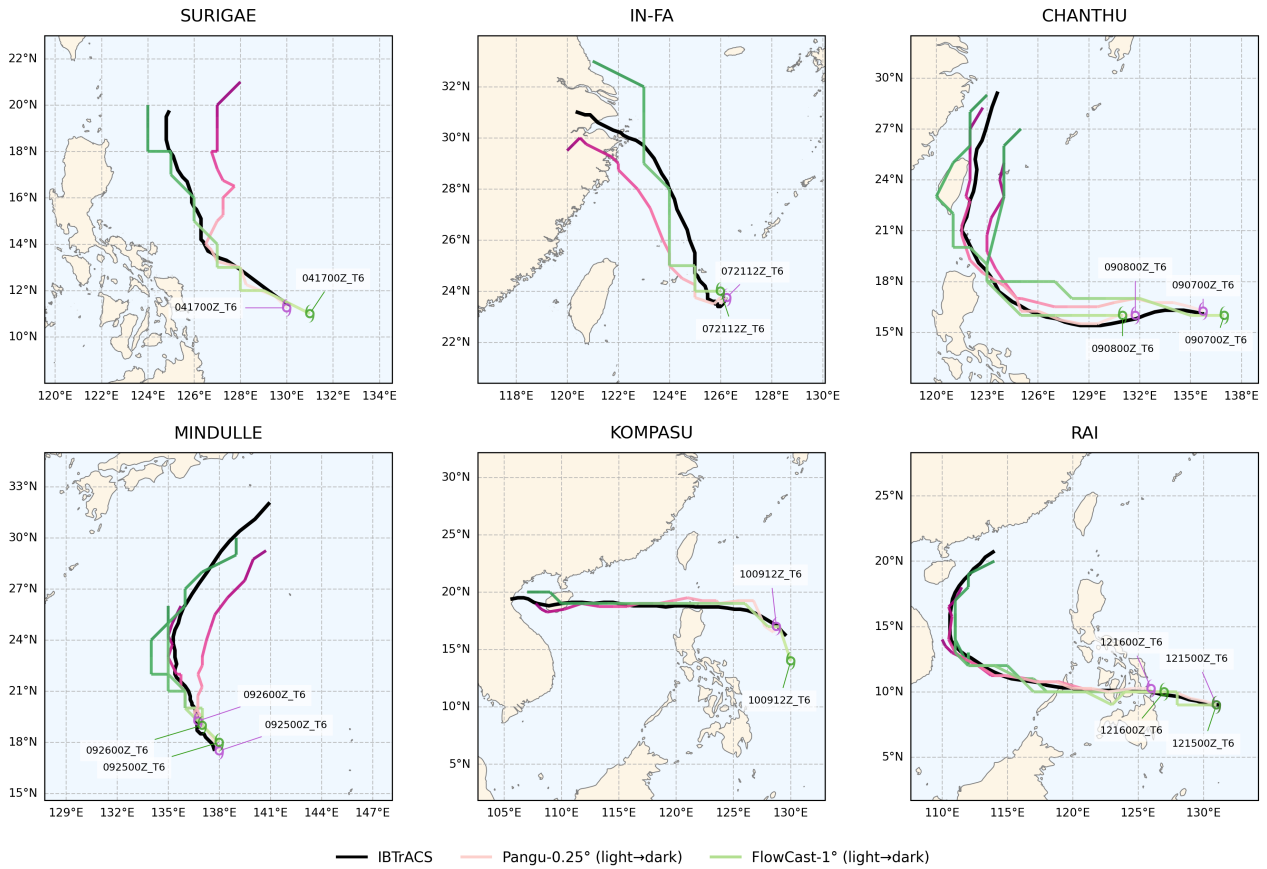


Figure 4. Observed IBTrACS tracks (black line) and predicted trajectories with 6-hour intervals from FlowCast-ODE 1° (green line) and 0.25° Pangu-Weather (purple line) for six tropical cyclones in 2021. Typhoon markers denote positions six hours after forecast initialization, and initialization times are annotated in the panels. Line colors transition from light to dark with increasing lead time.

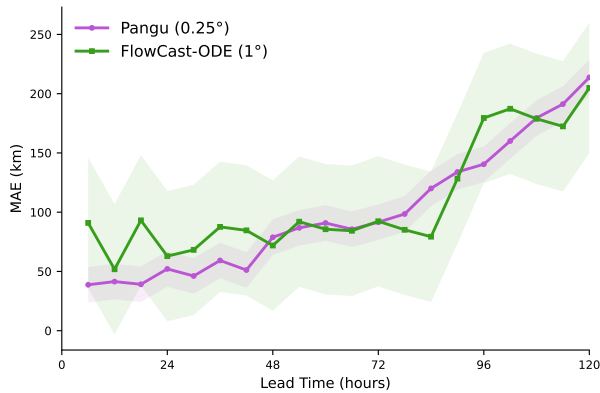


Figure 5. Comparison of the MAE for six tropical cyclone track forecasts in 2021 over a 120-hour forecast period for both FlowCast-ODE and the 0.25° Pangu-Weather. The shaded area indicates the spatial extent represented by each model's grid.

3.4. Temporal continuity of Atmospheric Energy

We examine the temporal evolution of kinetic energy and internal energy using a case initialized at 00 UTC on 21 July 2021. Figure 6 shows the 5-day time series of ERA5 at 0.25° and 1° resolution, together with forecasts from Pangu-Weather at 0.25° (produced by the officially released model) and FlowCast-ODE at 1°.

For kinetic energy, both the 0.25° and 1° ERA5 data exhibit continuous evolution within each data assimilation window, but discontinuities appear between successive windows. FlowCast-ODE produces relatively smoother energy trajectory that closely follow the ERA5 trend, while Pangu-Weather, due to its hierarchical multi-model stitching strategy, shows fluctuations, and also a gradual underestimation of kinetic energy compared to ERA5. For internal energy, the 0.25° ERA5 values are consistently higher than those at 1°, with discontinuities also arising from assimilation cycles. Both FlowCast-ODE and Pangu-Weather underestimate internal energy relative to ERA5 at their respective resolutions.

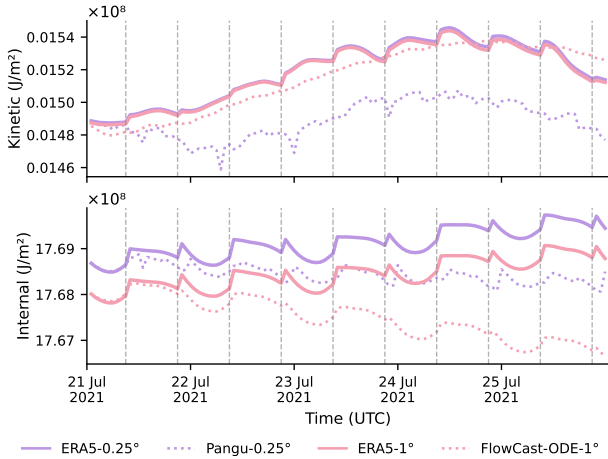


Figure 6. Time series of kinetic energy (top) and internal energy (bottom) over a 5-day period initialized at 00 UTC on 21 July 2021. Depicted are ERA5 at 0.25° (solid purple) and 1° resolution (solid pink), along with forecasts from Pangu-Weather at 0.25° (dashed purple) and FlowCast-ODE at 1° (dashed pink). ERA5 shows spurious jumps at the boundaries of 12-hour assimilation windows, while FlowCast-ODE exhibits smoother temporal trajectory and Pangu-Weather forecasts display fluctuations.

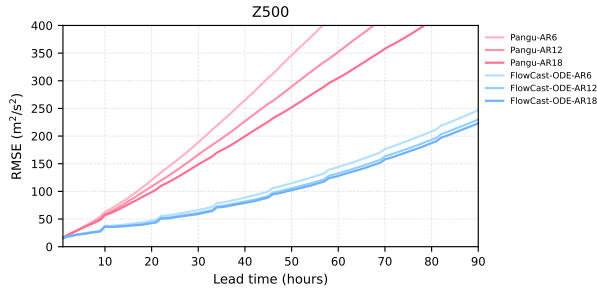


Figure 7. Latitude-weighted RMSE of Z500 over a 5-day forecast horizon for different autoregressive (AR) steps. Results are shown for the 1-hour Pangu model and FlowCast-ODE after AR6, AR12, and AR18 steps, evaluated on July 2021.

FlowCast-ODE again demonstrates better temporal continuity, whereas Pangu-Weather exhibits fluctuations.

Notably, both models track the kinetic and internal energy of ERA5 closely during the first assimilation window, but the discrepancies increase after each successive window, highlighting the influence of assimilation-induced discontinuities in ERA5 on model forecasts. Additional case studies are provided in the Appendix E.2.

3.5. Ablation Studies

Comparison of Multi-step Fine-tuning Figure 7 compares the 500 hPa geopotential RMSE of the Pangu-Weather 1-hour model and FlowCast-ODE across multiple autore-

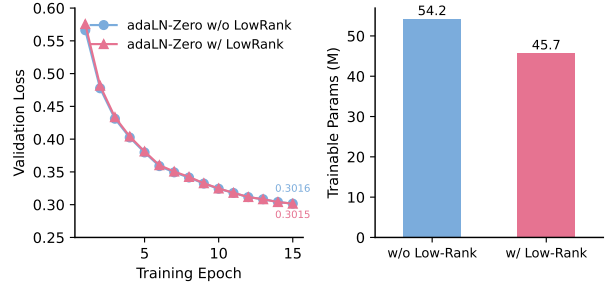


Figure 8. Validation loss curves (left) and model parameters (right) for FlowCast-ODE using adaLN-Zero temporal modulation with and without Low-Rank decomposition. Both models are trained on ERA5 data from 2010–2019, and the curves are shown across training epochs.

gressive steps. While fine-tuning the Pangu-Weather 1-hour model reduces long-term RMSE significantly, it still falls short of FlowCast-ODE’s performance. This highlights the advantage of FlowCast-ODE’s framework for maintaining accuracy in long-horizon hourly forecasts.

Low-Rank adaLN-Zero Figure 8 shows validation loss curves for FlowCast-ODE with adaLN-Zero modulation, comparing the full-rank (54.2M parameters) and Low-Rank (45.7M parameters) variants. The Low-Rank model achieves comparable, and slightly better loss throughout training, demonstrating that the Low-Rank design reduces model size without sacrificing predictive performance.

4. Conclusion

In this study, we introduced FlowCast-ODE, a novel and lightweight deep learning framework for continuous hourly weather forecasting. FlowCast-ODE first models atmospheric evolution as a conditional continuous flow at 6-hour intervals, and then refines hourly forecasts via an ODE solver. Experiments demonstrate that FlowCast-ODE surpasses strong baselines, achieving lower RMSE and better preservation of spectral power, maintaining fine-scale spatial details. Its capability in extreme weather prediction, such as tropical cyclone track forecasts, is comparable to that of the state-of-the-art 0.25° Pangu-Weather model. These results demonstrate FlowCast-ODE’s ability to deliver accurate and stable hourly forecasts.

While FlowCast-ODE demonstrates strong performance, its current resolution limits its ability to capture small-scale extreme events, and it lacks native support for ensemble forecasting for uncertainty quantification. Additionally, spectral energy conservation could be further optimized for long-term stability. Future work will focus on addressing these issues. Overall, FlowCast-ODE represents an important step toward accurate and continuous hourly weather prediction.

Acknowledgements

Impact Statement

This paper presents work on achieving accurate and continuous hourly weather forecasts using dynamic flow matching and ODE-based integration. Our approach demonstrates that a single model with comparable parameters can achieve what currently requires four separate models in Pangu-Weather, significantly improving computational efficiency. We also highlight the temporal discontinuities in ERA5 reanalysis data caused by the 12-hour assimilation cycle, which are important to consider for high-frequency forecasting.

References

- Ba, J. L., Kiros, J. R., and Hinton, G. E. Layer normalization. *arXiv preprint arXiv:1607.06450*, 2016.
- Bauer, P., Thorpe, A., and Brunet, G. The quiet revolution of numerical weather prediction. *Nature*, 525(7567):47–55, 2015. doi: 10.1038/nature14956.
- Bi, K., Xie, L., Zhang, H., Chen, X., Gu, X., and Tian, Q. Accurate medium-range global weather forecasting with 3D neural networks. *Nature*, 619(7970):533–538, 2023.
- Bodnar, C., Bruinsma, W. P., Lucic, A., Stanley, M., Allen, A., Brandstetter, J., Garvan, P., Riechert, M., Weyn, J. A., Dong, H., Gupta, J. K., Thambiratnam, K., Archibald, A. T., Wu, C.-C., Heider, E., Welling, M., Turner, R. E., and Perdikaris, P. A foundation model for the Earth system. *Nature*, 641:1180–1187, 2025.
- Bouallègue, Z. B., Clare, M. C. A., Magnusson, L., Gascon, E., Maier-Gerber, M., Janoušek, M., Rodwell, M., Pinault, F., Dramsch, J. S., Lang, S. T. K., et al. The rise of data-driven weather forecasting: A first statistical assessment of machine learning-based weather forecasts in an operational-like context. *Bulletin of the American Meteorological Society*, 105:E864–E883, 2024.
- Chen, K., Han, T., Ling, F., Gong, J., Bai, L., Wang, X., Luo, J.-J., Fei, B., Zhang, W., Chen, X., Ma, L., Zhang, T., Su, R., Ci, Y., Li, B., Yang, X., and Ouyang, W. The operational medium-range deterministic weather forecasting can be extended beyond a 10-day lead time. *Communications Earth & Environment*, 6:518, 2025.
- Chen, L., Zhong, X., Zhang, F., Cheng, Y., Xu, Y., Qi, Y., and Li, H. FuXi: A cascade machine learning forecasting system for 15-day global weather forecast. *npj Climate and Atmospheric Science*, 6(1):190.
- Chen, R. T. Q., Rubanova, Y., Bettencourt, J., and Duvenaud, D. Neural ordinary differential equations. In *Advances in Neural Information Processing Systems*, pp. 6571–6583. NeurIPS, 2018.
- Dinh, L., Krueger, D., and Bengio, Y. NICE: Non-linear independent components estimation. *arXiv preprint arXiv:1410.8516*, 2014.
- ECMWF. IFS Documentation CY47R3 - Part IV Physical processes. Technical report, European Centre for Medium-Range Weather Forecasts, 2020. URL <https://www.ecmwf.int/en/publications/ifs-documentation>.
- Esser, P., Kulal, S., Blattmann, A., Entezari, R., Müller, J., Saini, H., Levi, Y., Lorenz, D., Sauer, A., Boesel, F., Podell, D., Dockhorn, T., English, Z., and Rombach, R. Scaling rectified flow transformers for high-resolution image synthesis. In *International Conference on Learning Representations*, 2024.
- Gao, Y., Wu, H., Shu, R., Dong, H., Xu, F., Chen, R., Yan, Y., Wen, Q., Hu, X., Wang, K., Wu, J., Li, Q., Xiong, H., and Huang, X. Oneforecast: A universal framework for global and regional weather forecasting. In *International Conference on Machine Learning*. PMLR, 2025.
- He, K., Zhang, X., Ren, S., and Sun, J. Deep residual learning for image recognition. In *Proceedings of the IEEE Conference on Computer Vision and Pattern Recognition (CVPR)*, 2016.
- Hersbach, H., Bell, B., Berrisford, P., Hirahara, S., Horányi, A., Muñoz-Sabater, J., Nicolas, J., Peubey, C., Radu, R., Schepers, D., et al. The era5 global reanalysis. *Quarterly Journal of the Royal Meteorological Society*, 146(730): 1999–2049, 2020.
- Ho, J., Jain, A., and Abbeel, P. Denoising diffusion probabilistic models. *arXiv preprint arXiv:2006.11239*, 2020.
- Iserles, A. *A First Course in the Numerical Analysis of Differential Equations*. Cambridge University Press, Cambridge, UK, 2009.
- Karras, T., Aittala, M., Lehtinen, J., Hellsten, J., Aila, T., and Laine, S. Analyzing and improving the training dynamics of diffusion models. *arXiv preprint arXiv:2312.02696*, 2023.
- Kingma, D. P. and Ba, J. Adam: A method for stochastic optimization. In *International Conference on Learning Representations*, 2015.
- Knapp, K. R., Kruk, M. C., Levinson, D. H., Diamond, H. J., and Neumann, C. J. The International Best Track Archive for Climate Stewardship (IBTrACS): Unifying Tropical Cyclone Data. *Bulletin of the American Meteorological Society*, 91(3):363–376, 2010.

- Knapp, K. R., Diamond, H. J., Kossin, J. P., Kruk, M. C., and Schreck, C. J. International Best Track Archive for Climate Stewardship (IBTrACS) Project, Version 4. Technical report, NOAA National Centers for Environmental Information, 2018.
- Kochkov, D., Yuval, J., Langmore, I., Norgaard, P., Smith, J., Mooers, G., Klöwer, M., Lottes, J., Rasp, S., Düben, P., Hatfield, S., Battaglia, P., Sanchez-Gonzalez, A., Willson, M., Brenner, M. P., and Hoyer, S. Neural general circulation models for weather and climate. *Nature*, 632: 852–858, 2024.
- Lam, R., Sanchez-Gonzalez, A., Willson, M., Wyrnsberger, P., Fortunato, M., Alet, F., Ravuri, S., Ewalds, T., Eaton-Rosen, Z., Hu, W., et al. Learning skillful medium-range global weather forecasting. *Science*, 382(6677):1416–1421, 2023.
- Lang, S., Alexe, M., Chantry, M., Dramsch, J., Pinault, F., Raoult, B., Clare, M. C. A., Lessig, C., Maier-Gerber, M., Magnusson, L., Bouallègue, Z. B., Nemesio, A. P., Dueben, P. D., Brown, A., Pappenberger, F., and Rabier, F. Aifs – ecmwf’s data-driven forecasting system. *arXiv preprint arXiv:2406.01465*, 2024.
- Langley, P. Crafting papers on machine learning. In Langley, P. (ed.), *Proceedings of the 17th International Conference on Machine Learning (ICML 2000)*, pp. 1207–1216, Stanford, CA, 2000. Morgan Kaufmann.
- Lim, S. H., Wang, Y., Yu, A., Hart, E., Mahoney, M. W., Li, X. S., and Erichson, N. B. Elucidating the design choice of probability paths in flow matching for forecasting. *arXiv preprint arXiv:2410.03229*, 2025.
- Ling, F., Ouyang, L., Larbi, B. R., Luo, J.-J., Han, T., Zhong, X., and Bai, L. Improving global weather and ocean wave forecast with large artificial intelligence models. *Science China Earth Sciences*, 67(12):3641–3654, 2024.
- Lipman, Y., Chen, R. T. Q., Ben-Hamu, H., Nickel, M., Le, M., Carlier, A., and Arya, P. Flow matching for generative modeling. In *International Conference on Learning Representations*, 2023.
- Liu, X., Gong, C., and qiang liu. Flow straight and fast: Learning to generate and transfer data with rectified flow. In *The Eleventh International Conference on Learning Representations*, 2023.
- Liu, Z., Lin, Y., Cao, Y., Hu, H., Wei, Y., Zhang, Z., Lin, S., and Guo, B. Swin transformer: Hierarchical vision transformer using shifted windows. In *Proceedings of the IEEE/CVF International Conference on Computer Vision*, pp. 9992–10002. IEEE, 2021.
- Loshchilov, I. and Hutter, F. Decoupled weight decay regularization. *International Conference on Learning Representations*, 2019.
- Mayer, J., Mayer, M., and Haimberger, L. Consistency and Homogeneity of Atmospheric Energy, Moisture, and Mass Budgets in ERA5. *Journal of Climate*, 34(10): 3955–3974, 2021.
- Nguyen, T., Brandstetter, J., Kapoor, A., Gupta, J. K., and Grover, A. Climax: A foundation model for weather and climate. *arXiv preprint arXiv:2301.10343*, 2023a.
- Nguyen, T., Shah, R., Bansal, H., Arcomano, T., Madireddy, S., Maulik, R., Kotamarthi, V., Foster, I., and Grover, A. Scaling transformer neural networks for skillful and reliable medium-range weather forecasting. *arXiv preprint arXiv:2312.03876*, 2023b.
- Paszke, A., Gross, S., Massa, F., Lerer, A., Bradbury, J., Chanan, G., Killeen, T., Lin, Z., Gimelshein, N., Antiga, L., Desmaison, A., Kopf, A., Yang, E., DeVito, Z., Raison, M., Tejani, A., Chilamkurthy, S., Steiner, B., Fang, L., Bai, J., and Chintala, S. Pytorch: An imperative style, high-performance deep learning library. In *Advances in Neural Information Processing Systems*, 2019.
- Pathak, J., Subramanian, S., Harrington, P., Raja, S., Chattopadhyay, A., Mardani, M., Kurth, T., Hall, D., Li, Z., Azizzadenesheli, K., Hassanzadeh, P., Kashinath, K., and Anandkumar, A. Fourcastnet: A global data-driven high-resolution weather model using adaptive fourier neural operators. *arXiv preprint arXiv:2202.11214*, 2022.
- Peebles, W. and Xie, S. Scalable diffusion models with transformers. In *Proceedings of the IEEE/CVF International Conference on Computer Vision*, pp. 4172–4182. IEEE, 2023.
- Pielke, R. A. and Carbone, R. E. Weather impacts, forecasts, and policy: An integrated perspective. *Bulletin of the American Meteorological Society*, 83(3):393–403, 2002.
- Price, I., Sanchez-Gonzalez, A., Alet, F., Andersson, T. R., El-Kadi, A., Masters, D., Ewalds, T., Stott, J., Mohamed, S., Battaglia, P., Lam, R., and Willson, M. Probabilistic weather forecasting with machine learning. *Nature*, 637 (8044):84–90.
- Rasp, S., Hoyer, S., Merose, A., Langmore, I., Battaglia, P., Russell, T., Sanchez-Gonzalez, A., Yang, V., Carver, R., Agrawal, S., Chantry, M., Ben Bouallegue, Z., Dueben, P., Bromberg, C., Sisk, J., Barrington, L., Bell, A., and Sha, F. Weatherbench 2: A benchmark for the next generation of data-driven global weather models. *Journal of Advances in Modeling Earth Systems*, 16(6), 2024.

- Ritchie, H., Tanguay, M., Thépaut, J.-N., Brunet, G., and Pellerin, P. Implementation of the semi-lagrangian method in a high-resolution version of the ecmwf forecast model. *Monthly Weather Review*, 123(2):489–514, 1995.
- Schreck, J., Sha, Y., Chapman, W., Kimpara, D., Berner, J., McGinnis, S., Kazadi, A., Sobhani, N., Kirk, B., and II, D. J. G. Community research earth digital intelligence twin (CREDIT). *arXiv preprint arXiv:2411.07814*, 2024.
- Sha, Y., Schreck, J. S., Chapman, W., and II, D. J. G. Improving AI weather prediction models using global mass and energy conservation schemes, 2025.
- Song, J., Meng, C., and Ermon, S. Denoising diffusion implicit models. In *International Conference on Learning Representations*, 2021.
- Song, J., Meng, C., and Ermon, S. Denoising diffusion implicit models. *arXiv preprint arXiv:2010.02502*, 2022.
- Verma, Y., Heinonen, M., and Garg, V. ClimODE: Climate and Weather Forecasting with Physics-informed Neural ODEs. In *Proceedings of the 12th International Conference on Learning Representations (ICLR 2024)*, 2024.
- Wedi, N. P. Increasing horizontal resolution in numerical weather prediction and climate simulations: Recent progress and challenges. *Quarterly Journal of the Royal Meteorological Society*, 140(683):1830–1844, 2014.
- White, P. Newsletter no. 102—winter 2004/05. Technical report, European Centre for Medium-Range Weather Forecasts, 2018.
- Yuan, P., Blewitt, G., Kreemer, C., Jiang, W., Liu, T., He, L., Shan, Q., Balidakis, K., Schuh, H., Wickert, J., and Deng, Z. A Global Assessment of Diurnal Discontinuities in ERA5 Tropospheric Zenith Total Delays Using 10 Years of GNSS Data. *Geophysical Research Letters*, 52(5): e2024GL113140, 2025.

A. Data Details

A.1. Dataset

We conduct experiments on the WeatherBench2 (Rasp et al., 2024) benchmark, which is a curated subset of the ERA5 (Hersbach et al., 2020) reanalysis dataset provided by the European Centre for Medium-Range Weather Forecasts (ECMWF). ERA5 is a global atmospheric reanalysis spanning from 1959 to the present, with a native spatial resolution of 0.25° latitude/longitude and 1-hour temporal intervals. It is produced using ECMWF’s HRES model (cycle 42r1) within a 4D-Var data assimilation framework, which combines forecasts with observations in 12-hour assimilation windows (21:00–09:00 and 09:00–21:00). We adopt the 1° resolution (corresponds to a grid size of 181×360) version of WeatherBench2. As summarized in Table 2, the dataset we used contains five atmospheric variables (Z, Q, T, U, V) at 13 pressure levels (50, 100, 150, 200, 250, 300, 400, 500, 600, 700, 850, 925, and 1,000 hPa), six surface variables (U10M, V10M, T2M, TD2M, MSLP, TP), as well as topographical features including geopotential height, land-sea mask, and soil type. For model development, the data is split into 1980–2019 for training, 2020 for validation, and 2021 for testing.

Table 2. List of variables used in the experiments

Type	Variable name	Short name	Unit
Atmospheric	Geopotential height	Z	$\text{m}^2 \text{s}^{-2}$
Atmospheric	Specific humidity	Q	kg kg^{-1}
Atmospheric	Temperature	T	K
Atmospheric	U component of wind	U	m s^{-1}
Atmospheric	V component of wind	V	m s^{-1}
Single	10-m u wind component	U10M	m s^{-1}
Single	10-m v wind component	V10M	m s^{-1}
Single	2-m temperature	T2M	K
Single	2-m dewpoint temperature	TD2M	K
Single	Mean sea level pressure	MSLP	Pa
Single	Total Precipitation	TP	kg m^3
Static	Geopotential at surface	Z	$\text{m}^2 \text{s}^{-2}$
Static	Land-sea mask	–	–
Static	Soil type	–	–
Static	Latitude	–	–
Static	Longitude	–	–
Clock	Local time of day	–	–
Clock	Elapsed year progress	–	–

A.2. Data Preprocessing

All variables were normalized prior to model training to ensure numerical stability and facilitate effective learning. Specifically, for each variable at each level, we calculated the mean and standard deviation using the training dataset spanning from 1980 to 2019. Normalization was performed by subtracting the corresponding mean and dividing by the standard deviation, resulting in zero-mean and unit-variance variables. For total precipitation, which typically exhibits a highly skewed distribution and strong imbalance, we applied a logarithmic transformation: $\hat{TP} = 10 \cdot \log_{10} (1 + 200 \cdot TP^{1.6})$.

A.3. Assimilation Window Discontinuities

The ERA5 reanalysis data are produced by ECMWF’s 4D-Var data assimilation system, which assimilates observations over 12-hour windows (09:00–21:00 UTC and 21:00–09:00 UTC). When examining RMSE evolution over a 120-hour forecast horizon, we observed sudden increases at the assimilation window boundaries, suggesting possible inconsistencies across the temporal edges. To investigate this further, we computed four vertically integrated components of atmospheric energy, which allowed us to identify temporal discontinuities in the ERA5 dataset. These abrupt changes in the atmospheric state pose challenges for iterative hourly forecasting, as hourly autoregressive models tend to accumulate significant errors

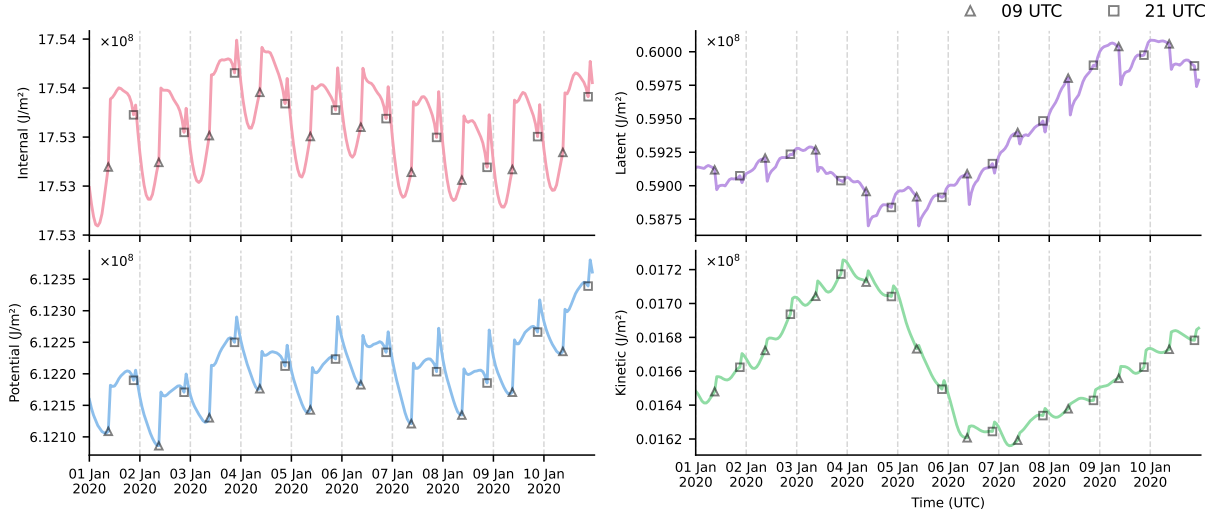


Figure 9. Time series of four atmospheric energy components (internal energy, latent heat energy, potential energy, and kinetic energy) together with the total energy, derived from ERA5 data. Triangles indicate values at 09 UTC, while square boxes represent values at 21 UTC, highlighting the discontinuities in the dataset.

near the assimilation boundaries. In contrast, models trained and operated at coarser temporal resolutions, such as 6-hour intervals, are less affected because their prediction steps effectively skip over the assimilation windows, avoiding these abrupt state changes.

The total energy of the air column is defined as ((Mayer et al., 2021; Sha et al., 2025)):

$$E = \frac{1}{g} \int_0^{p_s} [(1 - q)c_v T_c + L_v(T_c)q + \phi + k] dp, \quad (13)$$

with the terms representing:

- Internal energy: $c_v T$, where c_v is the specific heat capacity of air at constant volume and T_c is the air temperature in Celsius.
- Latent heat energy: $L_v(T_c)q$, with the temperature-dependent latent heat of vaporization $L_v(T_c)$, is defined according to Part IV of the IFS documentation (ECMWF, 2020), and q is the specific humidity.
- Potential energy: ϕ , the geopotential.
- Kinetic energy: $k = \frac{1}{2}(u^2 + v^2)$, defined in terms of the horizontal velocity components of the air parcel.

Here, g is the gravitational acceleration. To provide further insight into the effects of temporal discontinuities, visualizations of these energy components are presented in Figure 9.

A.4. IBTrACS

To assess tropical cyclone track forecasts, we utilize the International Best Track Archive for Climate Stewardship (IBTrACS) dataset (Knapp et al., 2010; 2018). IBTrACS integrates best-track data from international meteorological agencies, offering a comprehensive time series of cyclone-eye coordinates (latitude and longitude), wind speeds, and central pressures. In this work, we focus on six 2021 typhoons from the West Pacific basin—SURIGAE, IN-FA, MINDULLE, CHANTHU, KOMPASU, and RAI—to evaluate forecast accuracy against observed tracks.

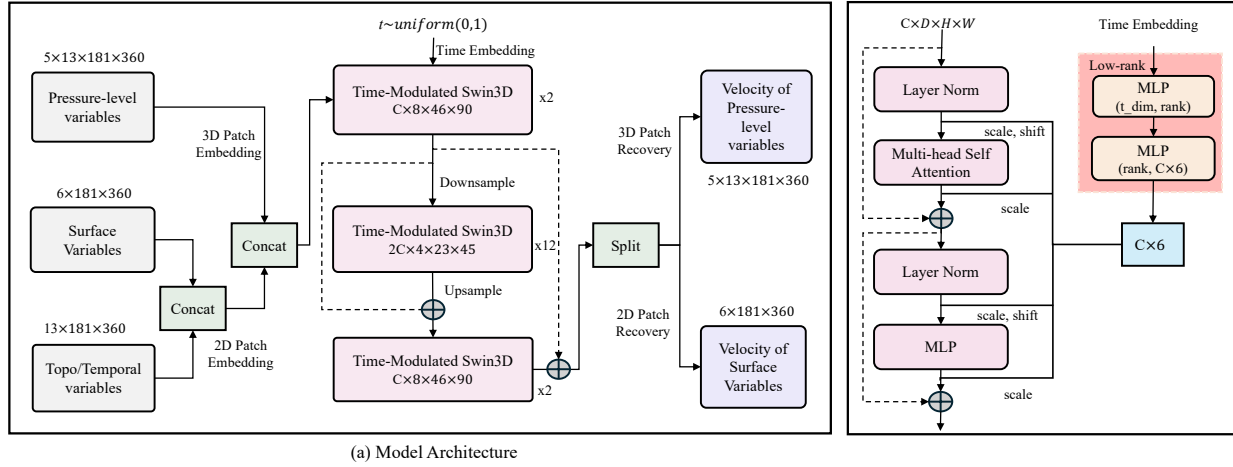


Figure 10. (a) the overall architecture of the velocity model (b) the low-rank time-modulated 3D Swin Transformer block.

B. Model Details

B.1. Model Architecture

The velocity model consists of three main components: patch embedding, time-modulated 3D Swin Transformer blocks, and patch recovery (Figure 10a).

Patch Embedding. The input data consists of 6 surface-level variables ($6 \times 181 \times 360$) and 5 pressure-level variables across 13 pressure levels ($5 \times 13 \times 181 \times 360$), along with 11 conditioning features (including the binary land–sea mask, surface geopotential, soil type, the sine and cosine of latitude and longitude, and the sine and cosine of local time of day and year progress, all normalized to $[0, 1)$). Pressure-level variables are processed via a 3D convolutional patch embedding with kernel size $2 \times 4 \times 4$ and stride $2 \times 4 \times 4$, producing a latent feature map of size $256 \times 7 \times 46 \times 90$. Surface-level variables and conditioning features are concatenated and embedded jointly using a 2D convolutional patch embedding with kernel size 4×4 and stride 4×4 , generating a feature map of size $256 \times 1 \times 46 \times 90$. The two embeddings are concatenated along the channel dimension, yielding a combined feature map of size $256 \times 8 \times 46 \times 90$, which is then fed into the subsequent 3D Swin Transformer blocks.

Time-Modulated 3D Swin Transformer Backbone. The embedded patches are processed by three consecutive layers containing 2, 12, and 2 3D Swin Transformer blocks (Liu et al., 2021), respectively. A downsampling operation is applied after the first layer, reducing the spatial size while doubling the number of channels to $512 \times 4 \times 23 \times 45$. A corresponding upsampling step is applied before the final layer, restoring the feature map to $256 \times 8 \times 46 \times 90$. Residual connections are applied such that the output of the first layer is added to the outputs of the second and third layers (He et al., 2016), allowing the model to retain low-level features across all subsequent layers and improving gradient flow. Each transformer block is equipped with a time modulation module, where the time is mapped into a sinusoidal embedding and then transformed by an MLP to provide temporal conditioning for the attention mechanism, thereby enabling adaptive handling of different times (Figure 10b).

Patch Recovery. The latent feature map is first split into two components of sizes $256 \times 1 \times 46 \times 90$ and $256 \times 7 \times 46 \times 90$, corresponding to surface-level and pressure-level features, respectively. Each component is then projected back to the original variable dimensions through a linear projection, restoring the spatial resolution and channel dimension for the final velocity field output.

The model architecture and parameters used in this study for Pangu-Weather and FlowCast-ODE are summarized in Table 3.

Table 3. Model architecture and capacity for Pangu-Weather and FlowCast-ODE.

Attribute	Pangu-Weather	FlowCast-ODE
Embedding size	256	256
Number of blocks	2/ 6/ 6/ 2	2/ 12/ 2
Patch size	[2, 4, 4]	[2, 4, 4]
Window size	[2, 5, 9]	[2, 5, 9]
Number of parameters	~51.0M	~45.7M

C. Training Details

C.1. Training objective

The model is trained by minimizing a weighted mean-squared-error (MSE) between the predicted velocity field and the target:

$$\mathcal{L}(\theta) = \frac{1}{C H W} \sum_{s=1}^C \sum_{i=1}^H \sum_{j=1}^W w_{\text{lat}}(i) w_{\text{lev}}(\ell_s) w_{\text{var}}(s) [v_{\theta}(x_t, t, c)_{s,i,j} - (X_{k+6} - X_k)_{s,i,j}]^2, \quad (14)$$

where

- $w_{\text{lat}}(i)$ — proportional to the surface area of the latitude–longitude grid cell at latitude φ , and normalized to have unit mean over the entire grid, ensuring uniform spatial weighting.
- $w_{\text{lev}}(\ell_s)$ — reduces the relative contribution of higher atmospheric levels where air density is lower.
- $w_{\text{var}}(s)$ — computed as the inverse of the time difference variance $(X_{k+6} - X_k)_s$ for each channel, standardizing the target to account for variable-dependent rates of temporal change.

C.2. Model Training

We train both Pangu-Weather and FlowCast-ODE using the same overall training framework, implemented in PyTorch (Paszke et al., 2019). For Pangu-Weather, we follow the implementation released in NVIDIA Modulus¹, training a 24-hour model on ERA5 data from 1980–2019 for 50 epochs. The optimizer is AdamW (Kingma & Ba, 2015; Loshchilov & Hutter, 2019) with weight decay of 0.1 and parameters ($\beta_1 = 0.9$, $\beta_2 = 0.95$), and the learning rate is scheduled using cosine annealing starting from 3×10^{-4} .

FlowCast-ODE training consists of two stages. In Stage 1, we train the 6-hour velocity model from scratch for 50 epochs using 1980–2019 ERA5 data. In Stage 2, we fine-tune the Stage 1 model for iterative hourly forecasting, performing fine-tuning runs for 6, 12, and 18 autoregressive (AR) steps. Each fine-tuning run uses 2000–2019 data and is trained for 5, 2, and 2 epochs, respectively, with learning rates 1×10^{-6} , 1×10^{-6} , and 3×10^{-7} . To reduce memory usage in Stage 2, gradient checkpointing is applied.

During training, each trajectory is rescaled to account for the near-linear increase in expected error variance with lead time τ , using the scaling factor $(1 + (\tau/24))^{-1/2}$. Additionally, we apply an Exponential Moving Average (EMA) of model parameters with a decay rate of 0.999 (Karras et al., 2023) for FlowCast-ODE, following common practice in flow matching. A full list of hyper-parameters for models is given in Table 4.

C.3. Training Time

Training the 24-hour Pangu-Weather model required approximately 70 hours using 4 NVIDIA A100 40GB GPUs. For FlowCast-ODE, the first-stage training on 6-hour intervals took about 66 hours, while the subsequent fine-tuning stage on hourly data required an additional 43 hours on the same hardware.

¹<https://github.com/NVIDIA/modulus>

Table 4. A full list of hyper-parameters used for the training of Pangu-Weather and FlowCast-ODE.

Hyper-parameter	Pangu-Weather	FlowCast-ODE Stage 1	FlowCast-ODE Stage 2
Forecast interval	24 h	6 h	1 h
Epochs	50	50	5 / 2 / 2
Batch size	16	16	4 / 4 / 4
Number of AR steps	1	1	6 / 12 / 18
Training data	1980–2019	1980–2019	2000–2019
Optimizer	AdamW	AdamW	AdamW
Weight decay	0.1	0.1	0.1
LR decay schedule	Cosine	Cosine	Constant
Peak LR	3×10^{-4}	3×10^{-4}	$1 \times 10^{-6} / 1 \times 10^{-6} / 3 \times 10^{-7}$
Gradient checkpointing	No	No	Yes

D. Experiments Details

D.1. Evaluation Metric

Latitude-weighted RMSE. For variable X_s at forecast time step k , the latitude-weighted RMSE is

$$\text{RMSE}_j(k) = \sqrt{\frac{1}{N_{\text{lat}} N_{\text{lon}}} \sum_{i=1}^{N_{\text{lat}}} \sum_{j=1}^{N_{\text{lon}}} w_{\text{lat}}(i) (X_s^{\text{pred}}(i, j, k) - X_s^{\text{true}}(i, j, k))^2}, \quad (15)$$

where $X_s^{\text{pred}}(i, j, k)$ and $X_s^{\text{true}}(i, j, k)$ denote the forecast and reference (ERA5) values at grid point (i, j) and time step k . The latitude weight $w_{\text{lat}}(i)$ is proportional to the surface area of the grid cell at latitude ϕ_i and normalized to have unit mean over the grid.

D.2. Spectral analysis

We evaluated the blurriness of forecasts using the power spectrum, implemented via the ZonalEnergySpectrum class from WeatherBench 2².

D.3. Typhoon Tracking

To track tropical cyclone centers, we employ a classical algorithm that identifies the local minimum of MSLP near a prescribed initial cyclone-eye location at 6-hour forecast intervals (White, 2018; Bi et al., 2023). A detected MSLP minimum is considered a tropical cyclone only if it satisfies the following dynamical and thermodynamical criteria:

- Maximum 850 hPa relative vorticity exceeding $5 \times 10^{-5} \text{s}^{-1}$ within a 278 km radius in the Northern Hemisphere (or below $-5 \times 10^{-5} \text{s}^{-1}$ in the Southern Hemisphere);
- Maximum 850–200 hPa thickness within a 278 km radius for extratropical systems;
- Maximum 10 m wind speed exceeding 8m s^{-1} within a 278 km radius over land.

Once the cyclone eye is confirmed, the tracker iteratively searches for subsequent positions within a 445 km vicinity. The procedure terminates when no local MSLP minimum meets the above conditions.

E. Supplementary Results

E.1. Spectrum

Supplementary results related to Section 3.2.2 are presented in Figure 11.

²https://github.com/google-research/weatherbench2/blob/main/weatherbench2/derived_variables.py

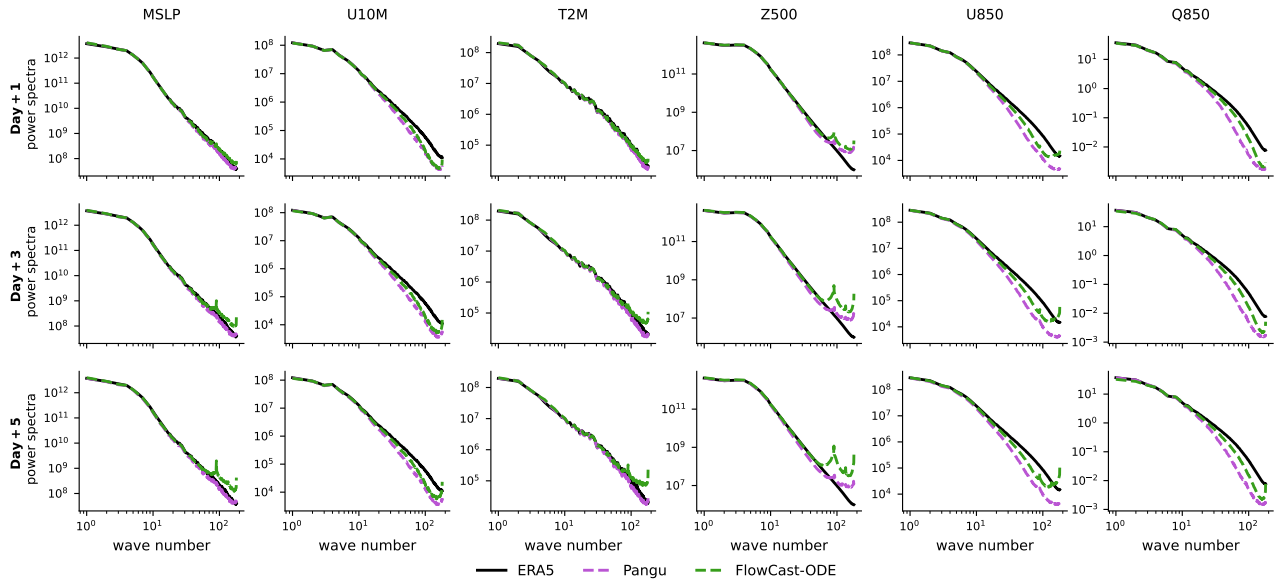


Figure 11. Latitude-averaged power spectra from 60°S to 60°N for ERA5 (black line), Pangu-Weather forecasts (purple dashed line), and FlowCast-ODE forecasts (green dashed line). Rows 1, 2, and 3 correspond to forecast days 1, 3, and 5, respectively.

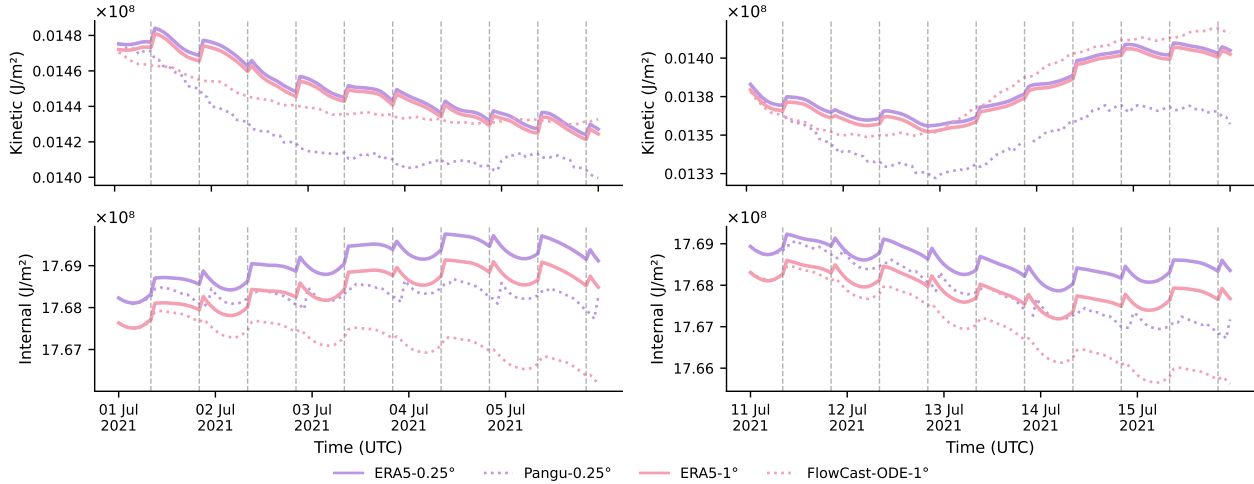


Figure 12. Same as Figure 6, but for 1–5 July 2021 (left) and 11–15 July 2021 (right).

E.2. Atmospheric Energy

Figure 12 shows additional cases of time series of kinetic and internal energy to further support the analysis in Section 3.4.

E.3. Forecast Visualization

In this final section, we provide visualization examples of the ground truth and the predictions produced by Pangu-Weather and FlowCast-ODE, both initialized with ERA5 data.

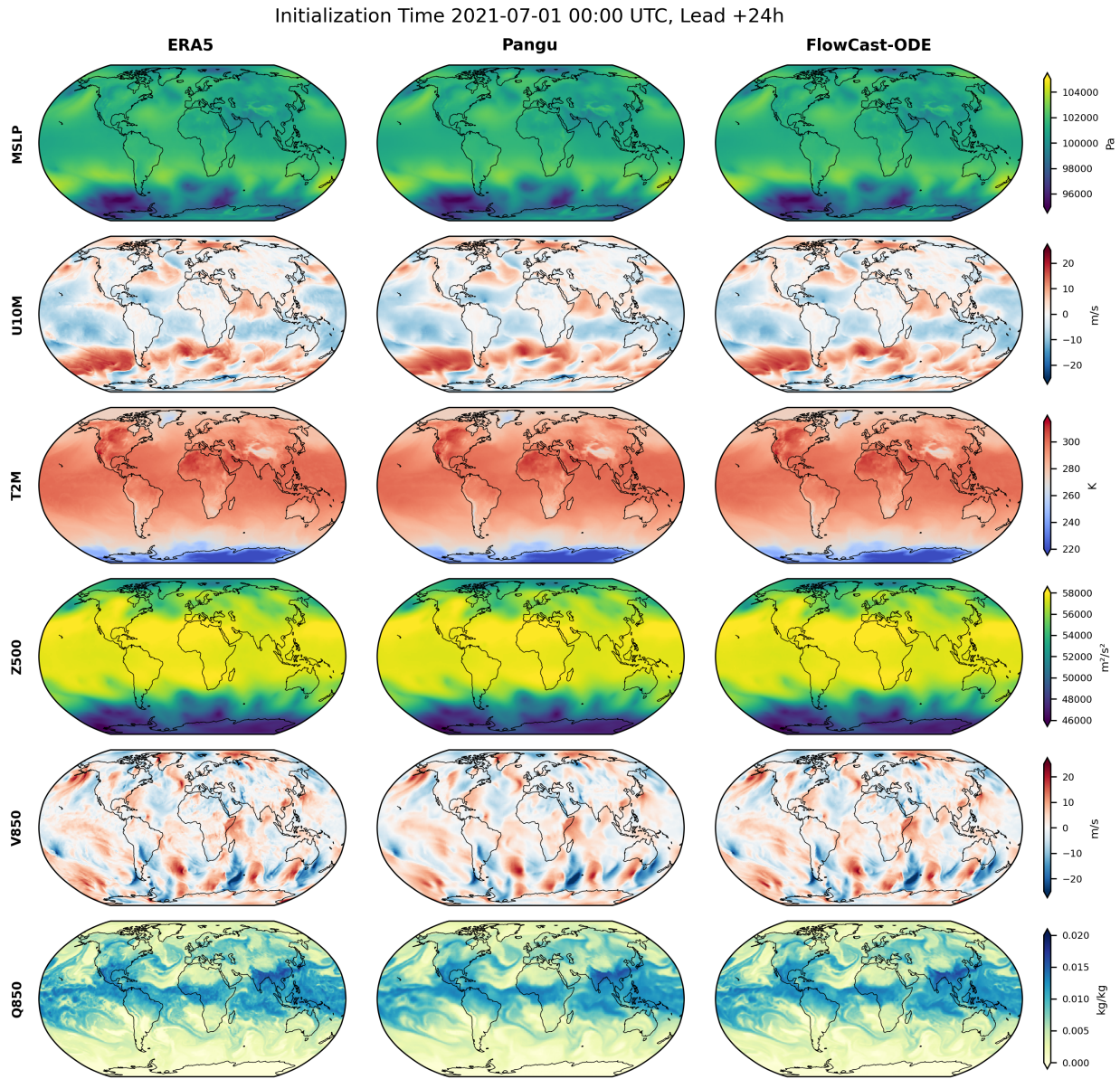


Figure 13. Visualization of 1-day forecast results. Forecasts initialized at 00:00 UTC on 1 July 2021.

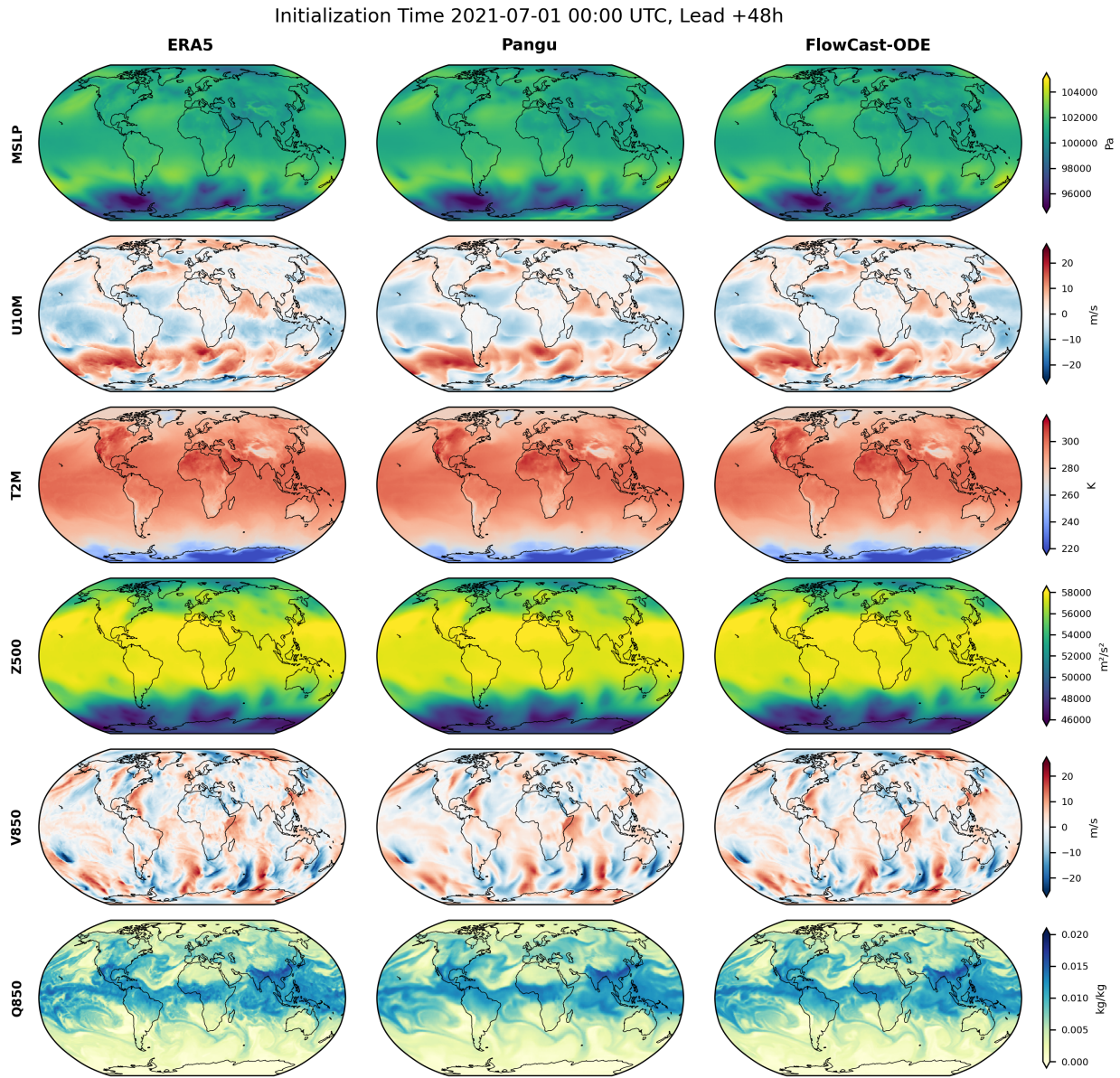


Figure 14. Visualization of 2-day forecast results. Forecasts initialized at 00:00 UTC on 1 July 2021.

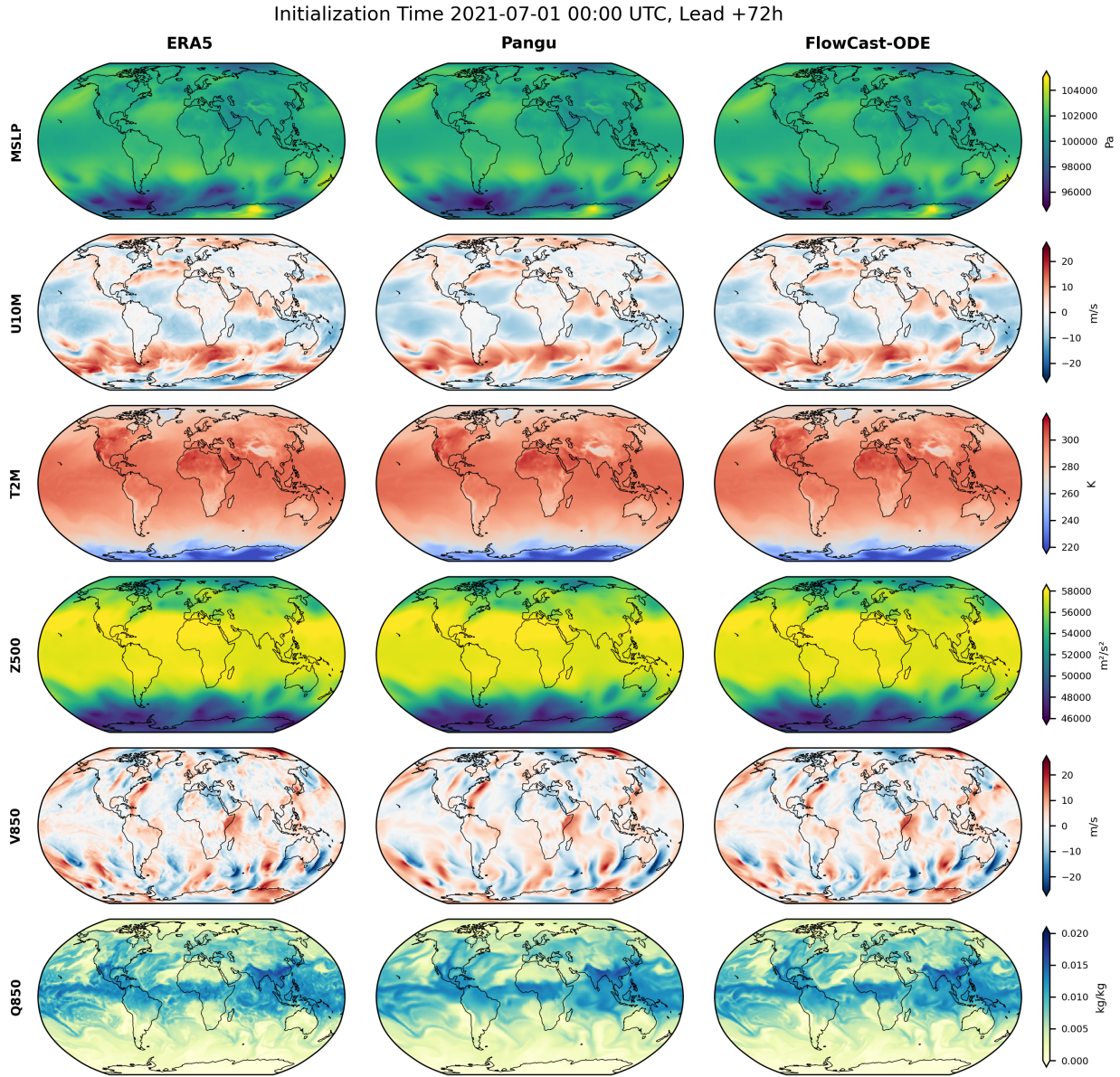


Figure 15. Visualization of 3-day forecast results. Forecasts initialized at 00:00 UTC on 1 January 2021.

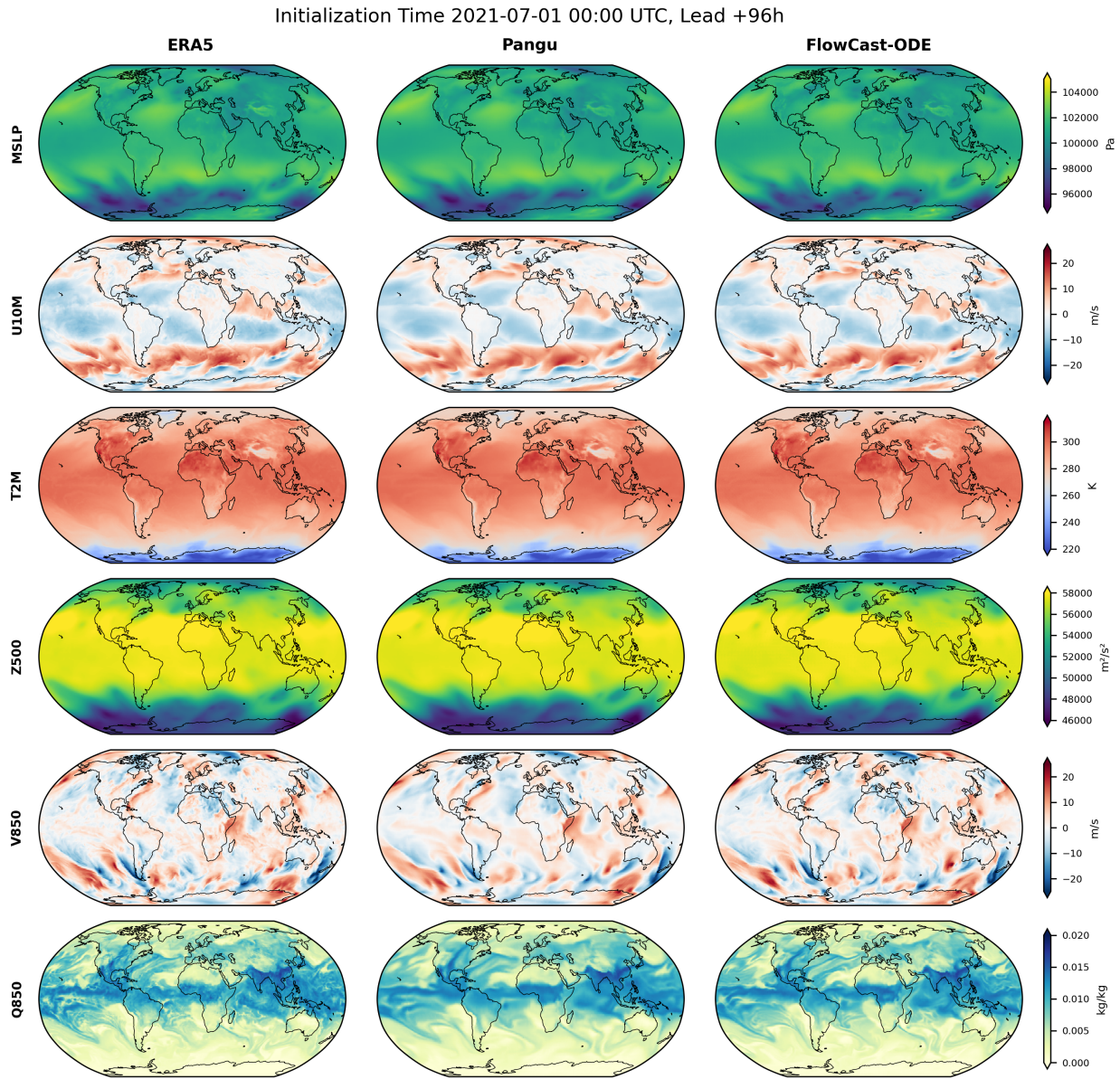


Figure 16. Visualization of 4-day forecast results. Forecasts initialized at 00:00 UTC on 1 July 2021.

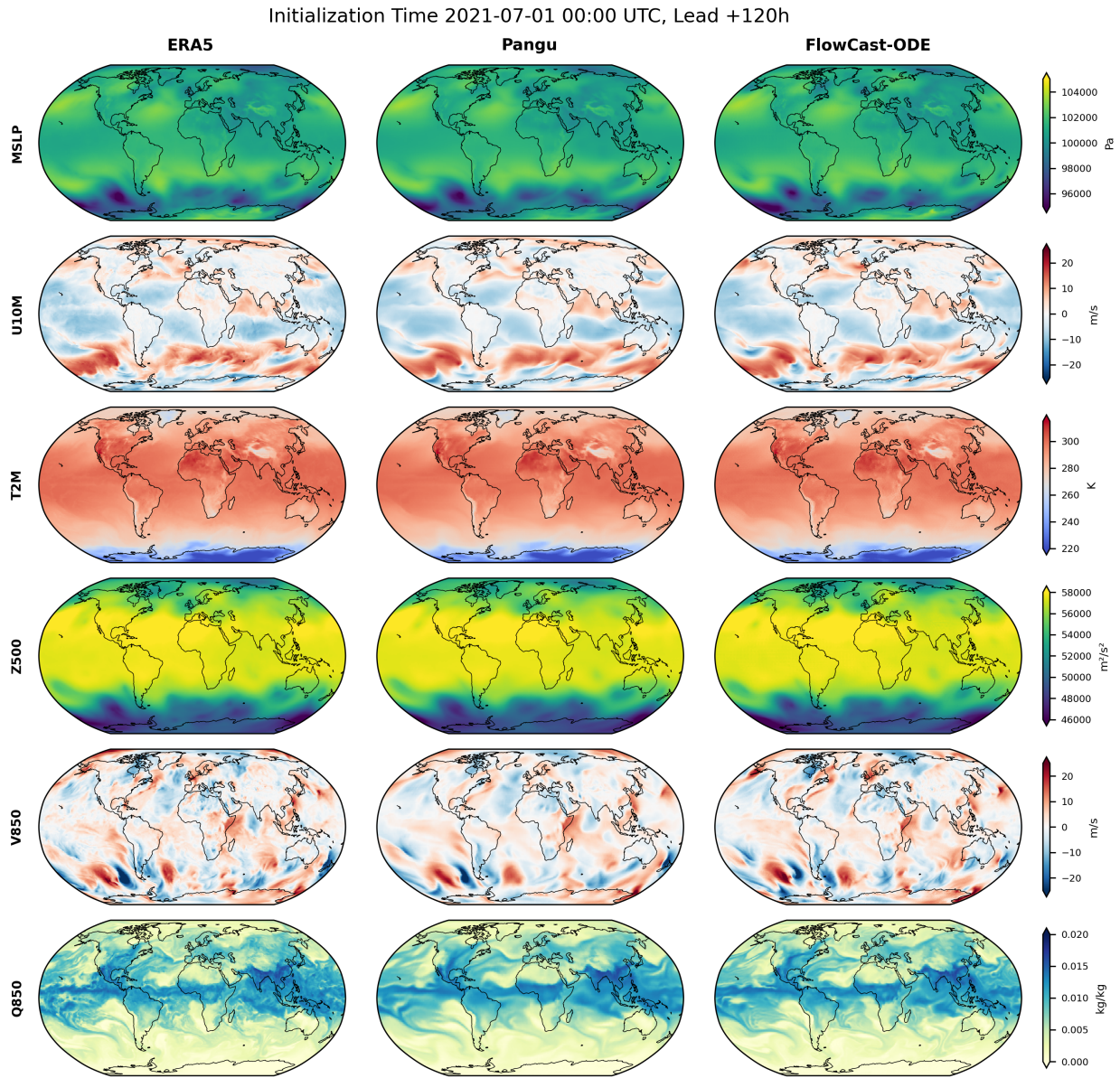


Figure 17. Visualization of 5-day forecast results. Forecasts initialized at 00:00 UTC on 1 July 2021.